
4 Modeling Glacier Flow

4.1 INTRODUCTION

The force that makes ice flow in the direction of decreasing surface elevation is the driving stress as defined in equation (3.21). This action is opposed by reactions, or resistive forces. Resistance to flow may originate at the glacier bed and at the lateral margins, or resistance may be associated with gradients in longitudinal stress (c.f. Section 3.1). Generally, because of the nonlinearity of the flow law, a velocity solution cannot be derived analytically, except in simplified cases where flow resistance is offered by only one of these potential sources. While this may appear overly restrictive, these limiting cases do apply to certain flow regimes found in Nature. Flow in the interior of ice sheets is mostly controlled by a balance between driving stress and drag at the glacier bed, and the corresponding lamellar flow model provides a good approximation of ice flow. On mountain glaciers, lateral drag arising from friction between the ice and valley walls may provide resistance to flow in addition to basal drag. In first approximation, this effect can be incorporated by introducing a shape factor to reduce basal drag in accordance with the role of lateral drag, but otherwise adopting the lamellar flow model. On Whillans Ice Stream in West Antarctica, basal friction is vanishingly small due to the presence of a water-saturated weak layer of sediment (for example, Whillans and van der Veen, 1997) and the driving stress is balanced almost entirely by lateral drag originating at the margins where the ice stream moves past nearly stagnant ice (van der Veen et al., 2007). This model of flow controlled by lateral drag also applies to floating ice shelves in comparatively narrow fjords. Finally, on free-floating ice shelves, the only resistance to flow is associated with gradients in longitudinal stress. In this chapter, these “end member” solutions are discussed.

Before continuing with the discussion of the various analytical velocity solutions, it is convenient to introduce a dimensionless vertical coordinate to account for changes in ice thickness, H , in the direction of flow:

$$s = \frac{h - z}{H}. \quad (4.1)$$

At the surface, $z = h$ and $s = 0$, whereas at the bed, $z = h - H$ and $s = 1$. By using this vertical coordinate, the model domain becomes a rectangular two-dimensional grid.

To find a relationship between horizontal gradients in the (x, z) coordinate system and those in the (x, s) coordinate system, consider [Figure 4.1](#). Let F be an arbitrary

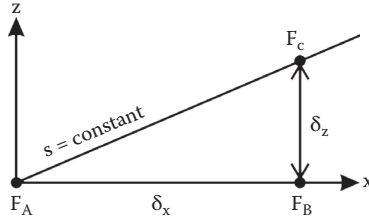


FIGURE 4.1 Transformation of gradients in the (x, z) coordinate system to those in the (x, s) coordinate system.

function of both coordinates x and z . The gradient in F evaluated along the surface $s = \text{constant}$ is related to that evaluated at $z = \text{constant}$, as

$$\frac{F_C - F_A}{\delta x} = \frac{F_C - F_B}{\delta z} \frac{\delta z}{\delta x} + \frac{F_B - F_A}{\delta x}. \quad (4.2)$$

In the limit of δx and δz approaching zero, this expression becomes

$$\left(\frac{\partial F}{\partial x} \right)_s = \left(\frac{\partial F}{\partial z} \right)_x \left(\frac{\partial z}{\partial x} \right)_s + \left(\frac{\partial F}{\partial x} \right)_z, \quad (4.3)$$

where the subscripts refer to the coordinate kept constant in calculating the gradients. From the definition of s it follows that $z = h - Hs$, and

$$\begin{aligned} \left(\frac{\partial z}{\partial x} \right)_s &= \frac{\partial h}{\partial x} - s \frac{\partial H}{\partial x} = \\ &= \Delta_s. \end{aligned} \quad (4.4)$$

Also,

$$\begin{aligned} \left(\frac{\partial F}{\partial z} \right)_x &= \left(\frac{\partial F}{\partial s} \right)_x \left(\frac{\partial s}{\partial z} \right)_x = \\ &= -\frac{1}{H} \left(\frac{\partial F}{\partial s} \right)_x. \end{aligned} \quad (4.5)$$

Substitution of these relations in equation (4.3) gives

$$\left(\frac{\partial F}{\partial x} \right)_z = \left(\frac{\partial F}{\partial x} \right)_s + \frac{\Delta_s}{H} \left(\frac{\partial F}{\partial s} \right)_x. \quad (4.6)$$

In the following, the subscripts on the derivatives are omitted where no confusion is likely.

In the (x, s) coordinate system, equation (3.8) expressing force balance in the x -direction in terms of full stresses, becomes (omitting the second term involving the gradient in the cross-flow direction, because plane flow is considered here)

$$\frac{\partial \sigma_{xx}}{\partial x} + \frac{\Delta_s}{H} \frac{\partial \sigma_{xx}}{\partial s} - \frac{1}{H} \frac{\partial \sigma_{xz}}{\partial s} = 0. \quad (4.7)$$

Substituting the partitioning of full stresses into lithostatic and resistive components, and multiplying by H , gives

$$H \frac{\partial R_{xx}}{\partial x} + \Delta_s \frac{\partial R_{xx}}{\partial s} - \rho g H \frac{\partial h}{\partial x} - \frac{\partial R_{xz}}{\partial s} = 0. \quad (4.8)$$

Integrating this expression with respect to s , from a general depth, s , in the ice, to the surface, $s = 0$, yields the following expression for the shear stress at that depth:

$$R_{xz}(s) = s \tau_{dx} - \frac{\partial}{\partial x} \left(\int_s^0 H R_{xx} d\bar{s} \right) + \Delta_s R_{xx}(s), \quad (4.9)$$

where the boundary condition (3.19) for a stress-free surface has been used. Equation (4.9) describes the balance of forces acting on an ice column extending from the surface to the depth s .

The next step is to express strain rates in terms of velocity gradients in the (x, s) coordinate system. Applying the transformation formula (4.6), along-flow stretching is given by

$$\begin{aligned} \dot{\epsilon}_{xx} &= \left(\frac{\partial u}{\partial x} \right)_z = \\ &= \left(\frac{\partial u}{\partial x} \right)_s + \frac{\Delta_s}{H} \left(\frac{\partial u}{\partial s} \right)_x. \end{aligned} \quad (4.10)$$

This expression cannot be evaluated directly because the last term on the right-hand side is related to the shear strain rate, which is unknown until the balance equation is solved.

To find an expression for the velocity gradient $(\partial u / \partial s)_x$ consider the definition of the shear strain rate

$$\dot{\epsilon}_{xz} = \frac{1}{2} \left[\left(\frac{\partial u}{\partial z} \right)_x + \left(\frac{\partial w}{\partial x} \right)_z \right]. \quad (4.11)$$

In terms of gradients in the (x, s) coordinate system, the two terms on the right-hand side are

$$\left(\frac{\partial u}{\partial z} \right)_x = -\frac{1}{H} \left(\frac{\partial u}{\partial s} \right)_x, \quad (4.12)$$

and

$$\left(\frac{\partial w}{\partial x}\right)_z = \left(\frac{\partial w}{\partial x}\right)_s + \frac{\Delta_s}{H} \left(\frac{\partial w}{\partial s}\right)_x. \quad (4.13)$$

The last term on the right-hand side of this equation is linked to the vertical strain rate:

$$\begin{aligned} \left(\frac{\partial w}{\partial s}\right)_x &= -H \left(\frac{\partial w}{\partial z}\right)_x = \\ &= -H \dot{\epsilon}_{zz} = \\ &= H \dot{\epsilon}_{xx}, \end{aligned} \quad (4.14)$$

where incompressibility of glacier ice has been invoked to link the vertical strain rate to the horizontal strain rate. Equation (4.11) can now be rewritten as

$$\left(\frac{\partial u}{\partial s}\right)_x = -H \left[2\dot{\epsilon}_{xz} - \left(\frac{\partial w}{\partial x}\right)_s - \Delta_s \dot{\epsilon}_{xx} \right]. \quad (4.15)$$

For most modeling applications, along-flow gradients in the vertical velocity are small and may be neglected. Similarly, even where the stretching rate may be significant, when multiplied by Δ_s the result will be small compared to the vertical shear strain rate, and equation (4.15) may be approximated by

$$\left(\frac{\partial u}{\partial s}\right)_x = -2H \dot{\epsilon}_{xz}. \quad (4.16)$$

With these preliminary manipulations out of the way, analytical solutions for simplified flow regimes can be derived.

4.2 LAMELLAR FLOW

In the simplest model for glacier flow, the driving stress is taken to be opposed entirely by basal drag; longitudinal stresses and lateral shear are neglected. This model is referred to as the lamellar flow model or the shallow ice approximation (for example, Greve and Blatter, 2009, Section 5.4).

If drag at the glacier base provides the sole resistance to flow, the force-balance equation (3.22) reduces to

$$\tau_{dx} = \tau_{bx}. \quad (4.17)$$

The shear stress at depth follows from consideration of the horizontal balance equation (4.9), with the last two terms on the right-hand side neglected:

$$R_{xz}(s) = s \tau_{dx}. \quad (4.18)$$

In other words, in the lamellar flow model, the shear stress, R_{xz} , always increases linearly from zero at the glacier surface to the maximum value, equal to the driving stress, at the glacier bed.

By definition of lamellar flow, the only nonzero strain rate is the vertical shearing rate, $\dot{\epsilon}_{xz}$. Using the constitutive relation (3.47) to link the shear stress to shear strain rate, the balance equation becomes

$$B \dot{\epsilon}_{xz}^{1/n} = s \tau_{dx}, \quad (4.19)$$

where B represents the viscosity factor and n the exponent in Glen's flow law (2.10). Except in the vicinity of ice divides, the vertical velocity, w , is usually small, and along-flow gradients in this quantity may be neglected. The vertical gradient in along-flow velocity is then related to the shear strain rate as (equation (4.16))

$$\left(\frac{\partial u}{\partial s} \right)_x = -2H \dot{\epsilon}_{xz}. \quad (4.20)$$

Combining equations (4.19) and (4.20) yields the following expression for the vertical gradient in the horizontal velocity, u :

$$\frac{\partial u}{\partial s} = 2AH \tau_{dx}^n s^n, \quad (4.21)$$

with $A = B^{-n}$ (c.f. Section 2.2).

The velocity at depth can be found by integrating equation (4.21) with respect to s from the bed ($s = 1$) to some level s in the ice:

$$u(s) = \frac{2AH}{n+1} (1 - s^{n+1}) \tau_{dx}^n + U_b, \quad (4.22)$$

where U_b represents the basal sliding velocity, that is, the velocity at the glacier bed. The first term on the right-hand side corresponds to the component of velocity associated with internal deformation.

The velocity at the glacier surface ($s = 0$) is

$$u(0) = \frac{2AH}{n+1} \tau_{dx}^n + U_b. \quad (4.23)$$

Setting the sliding velocity equal to zero, the deformational component of velocity at depth can also be written as

$$u(s) = u(0)(1 - s^{n+1}). \quad (4.24)$$

With $n = 3$, this expression shows that the velocity from internal deformation increases with the fourth power of depth below the surface. Most shearing is concentrated near the glacier base, as shown in [Figure 4.2](#).

In deriving the horizontal velocity profile, the assumption is made that the along-flow gradient in the vertical velocity, w , is negligible. This does not necessarily imply that the vertical velocity itself is negligible, and an expression for w can be derived

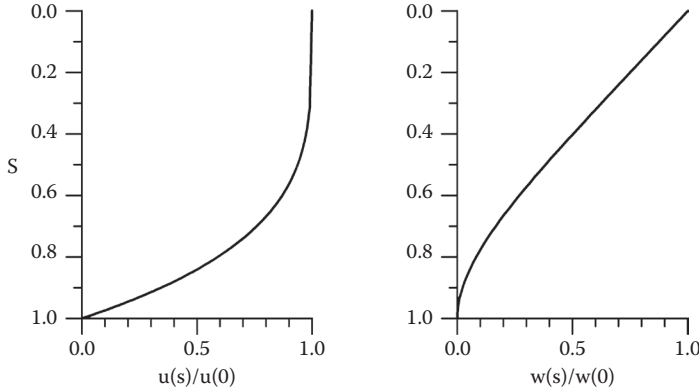


FIGURE 4.2 Horizontal (left panel) and vertical (right panel) component of velocity scaled to the surface velocity as a function of dimensionless depth, for the lamellar-flow model (using $n = 3$ for the exponent in the constitutive relation).

from the incompressibility criterion, which in the (x, s) coordinate system reads as (equations (4.14) and (4.10))

$$\left(\frac{\partial w}{\partial s} \right)_x = \left(\frac{\partial u}{\partial x} \right)_s + \frac{\Delta_s}{H} \left(\frac{\partial u}{\partial s} \right)_x, \quad (4.25)$$

where subscripts refer to the coordinate kept constant in evaluating the derivatives, and

$$\Delta_s = \frac{\partial h}{\partial x} - s \frac{\partial H}{\partial x}. \quad (4.26)$$

For a typical glacier, $\Delta_s/H \approx 10^{-5} - 10^{-6}$ and the second term in equation (4.25) may be neglected. Substituting the solution for the horizontal velocity gives the variation with depth of the vertical velocity

$$\left(\frac{\partial w}{\partial s} \right)_x = \frac{\partial u(0)}{\partial x} [1 - s^{n+1}]. \quad (4.27)$$

Setting the vertical velocity at the bed equal to zero, this expression can be integrated from the bed ($s = 1$) to some level s in the ice to yield

$$w(s) = -\frac{n+1}{n+2} \frac{\partial u(0)}{\partial x} \left[1 - s \left(\frac{n+2}{n+1} - \frac{s^{n+1}}{n+1} \right) \right]. \quad (4.28)$$

The vertical velocity at the surface is

$$w(0) = -\frac{n+1}{n+2} \frac{\partial u(0)}{\partial x}, \quad (4.29)$$

and the profile of the vertical velocity can be written as

$$w(s) = w(0) \left[1 - s \left(\frac{n+2}{n+1} - \frac{s^{n+1}}{n+1} \right) \right]. \quad (4.30)$$

This profile is shown in the right panel of [Figure 4.2](#) and indicates that the vertical velocity decreases approximately in a linear fashion with depth below the surface.

An important quantity needed in depth-averaged models is the vertical-mean velocity, U . Averaging equation (4.22) over the depth of the glacier gives

$$U = \frac{2AH}{n+2} \tau_{dx}^n + U_b. \quad (4.31)$$

The ice flux through a vertical section of unit width and extending from the base to the surface is given by HU and can be calculated from the glacier geometry (first term on the right-hand side) and a sliding relation for the sliding velocity, U_b .

The flow model described above is often referred to as *lamellar* or *laminar flow* and was first derived by Nye (1952a). The term *lamellar* is preferred to avoid any possible suggestion that glacier flow can become turbulent, as laminar fluid flow in a channel can become turbulent if the Reynolds number surpasses a critical value. To recapitulate, the most important assumptions of the lamellar model are that (1) basal drag is the only resistance to flow, (2) $\dot{\epsilon}_{xz}$ is the only nonzero strain rate, and (3) the ice is isothermal so that the rate factor, A , may be taken constant with depth. Under these constraints, which imply that the glacier geometry must be simple, with the upper and lower surfaces varying slowly in the direction of flow (that is, the glacier must resemble a plane slab), successive depth layers glide over one another similar to a deck of cards.

In the modeling community, the lamellar flow solution has become known as the Shallow Ice Approximation (SIA), in recognition of the fact that horizontal scales in glaciers and ice sheets are one or more orders of magnitude greater than the vertical scale. This allows introduction of typical quantities that are used as scaling parameters for physical variables and render the governing equations dimensionless. In particular, the horizontal coordinate, x , is nondimensionalized by dividing by the length scale (glacier length or half-width), L , while the dimensionless vertical coordinate is z/H . This introduces the small aspect ratio, H/L , as multiplier for some terms in the governing equations, allowing identification of higher-order terms that are likely to be small and that may be neglected in first approximation. A formal and rigorous treatment of scaling the force balance equations is presented in Hutter (1983) and Greve and Blatter (2009) and shows that, while the formal approach is decidedly more complex and lengthier than the intuitive discussion presented in this section, the resulting solution for the velocity distribution in glaciers is essentially the same.

Real glaciers are much more complex than assumed in the lamellar flow model. However, full calculations of stresses at depth for actual glaciers indicate that the shear stress, R_{xz} , increases almost linearly with depth, even where the driving stress is not entirely balanced by drag at the glacier base (for example, Section 4.3). This

means that the lamellar-flow solution is a useful approximation for the large-scale flow, provided that the driving stress in equations (4.22) and (4.31) is replaced by basal drag, τ_{bx} , if other resistive stresses are important. On this zero-order solution, small-scale perturbations may be super-imposed.

The lamellar flow model predicts an upper limit to the surface velocity associated with internal deformation. Equation (4.23) allows the surface velocity to be calculated from the glacier geometry or, better, from basal drag. An associated quantity that allows for comparison of different glaciers is the surface velocity from internal deformation divided by the ice thickness:

$$\frac{u(0)}{H} = \frac{A}{2} \tau_{bx}^3,$$

(4.32)

using $n = 3$ for the exponent in the flow law. For a given basal drag, the upper limit of this quantity can be readily calculated by using the value for a rate factor A that corresponds to ice temperatures close to the melting point. In Figure 4.3 this upper

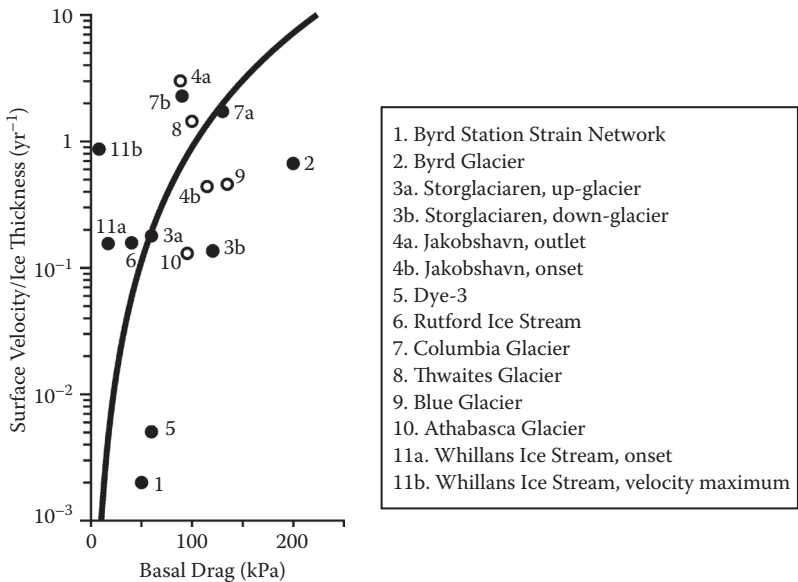


FIGURE 4.3 Relation between surface velocity divided by ice thickness, and basal drag, for various glaciers. Open circles indicate that basal drag is estimated from the driving stress, and filled circles refer to glaciers for which basal drag was estimated from balance of forces. The curve represents the upper limit to the deformational velocity, calculated from equation (4.24) using a rate factor corresponding to ice near the melting temperature. (Compiled from the following data sources: (1) Van der Veen and Whillans, 1989b; (2) Whillans et al., 1989; (3) Hooke et al., 1989; (4) Echelmeyer and Harrison, 1990 and Bindshadler, 1984; (5) Van der Veen and Whillans, 1990; (6) Frolich and Doake, 1988 and Frolich et al., 1987; (7) Van der Veen and Whillans, 1993; (8) McIntyre, 1985; (9) Engelhardt et al., 1978; (10) Raymond, 1969 quoted in Kamb, 1970; (11) Van der Veen, 1999b, Section 5.8.)

limit is shown as the solid curve. Also plotted in this figure is the ratio of the measured surface velocity and the ice thickness as a function of basal drag estimated for various glaciers. The curve divides the glaciers in two categories, namely, those that are definitely sliding over their bed (represented by the points on the left of the curve, such as 11a and 11b), and those that are flowing by internal deformation only (points to the right of the curve; for example, 2 and 5). Points that lie close to the theoretical curve represent glaciers where both basal sliding and internal deformation contribute to the flow.

4.3 INCLUDING LATERAL DRAG

Mountain glaciers generally flow through valleys that may partially impede the flow of the glacier. The friction generated between the moving ice and the rock walls provides resistance to flow, and the driving stress is supported by lateral drag (or side-wall friction) as well as drag at the glacier base. The effect of lateral drag on the flow of a valley glacier can be clearly seen in Figure 4.4, which shows contours of surface velocity obtained from repeat aerial photogrammetry of Columbia Glacier in Alaska. The glacier reaches its maximum speed near the center, and the velocity decreases toward both lateral margins. Transects of velocity are very similar to the depth profile shown in Figure 4.2, with the centerline corresponding to the glacier surface.

Where lateral drag is important, both shear stresses, R_{xz} and R_{xy} , must be included in the force-balance equations. Because of the nonlinear constitutive relation, a solution can be found only for a few exceptional cases, namely, a glacier in a circular basin (or nearly circular basin; Nye, 1965c), a very deep basin (in which case basal

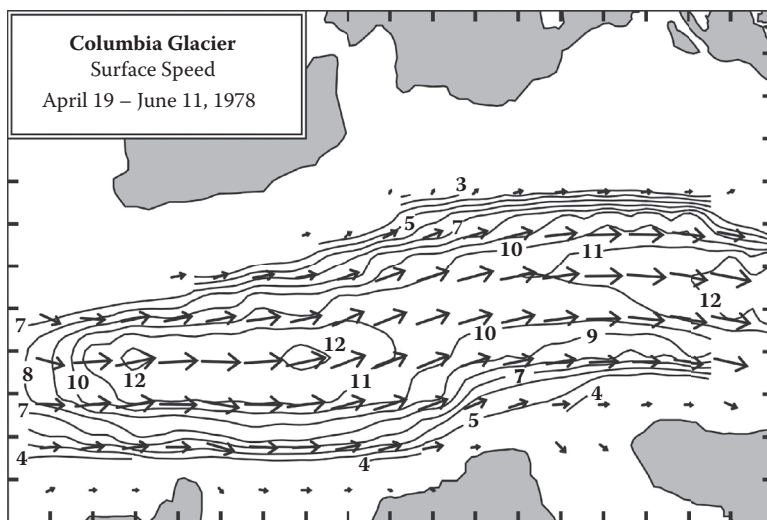


FIGURE 4.4 Surface speed on Columbia Glacier, Alaska, derived from repeat aerial photogrammetry. Speeds are in 100 m/yr and the contour interval is 100 m/yr. Shading represents bare rock.

drag and the vertical shear stress, R_{xz} , may be neglected), or a very wide glacier (in which case lateral drag may be neglected, except close to the margins, and the solution for the inner portion of the glacier reduces to the lamellar-flow solution discussed in Section 4.2). For more realistic geometries, the flow in a cross-section of a valley glacier must be found numerically as done by Nye (1965c) in what is perhaps the first numerical modeling study in glaciology.

The model used here to find the stress distribution in a cross-section is similar to the model described in Van der Veen (1989), except that the glacier geometry varies in the transverse direction rather than in the direction of flow. That is, the ice thickness, H , is assumed to be a function of the cross-flow coordinate, y , but constant in the flow direction, x . The surface elevation, h , is a function of the flow direction only, such that the surface slope, $\partial h/\partial x$, is constant in the direction of flow, and also taken constant across the width of the glacier. For the present discussion of results, the numerical details of this solution scheme are not important (the interested reader can find these details in Van der Veen, 1999b, Section 5.4). Similar results are obtained using off-the-shelf finite element solvers. Zero velocity is prescribed at the lower boundary.

Results of calculations for rectangular and parabolic channels are shown in [Figures 4.5](#) and 4.6. The parabolic cross-sectional profile is chosen such that the thickness at the margins ($y = \pm W$) is one-tenth of the ice thickness at the center, H_o , and

$$H(y) = H_o \left(1 - 0.9 \left(\frac{y}{W} \right)^2 \right). \quad (4.33)$$

This profile differs somewhat from that of Nye (1965c), who considered parabolic cross-sections with zero ice thickness at the margins. The parabolic profile is probably more representative of real valley basins. The examples shown are for basins with a half-width to centerline depth ratio of 4 ([Figure 4.5](#)) and 10 ([Figure 4.6](#)).

The upper panels in [Figures 4.5](#) and 4.6 show the normalized driving stress, T_d , normalized basal resistance, T_b , and normalized resistance from lateral drag, T_s . Following Nye (1965c), stresses are normalized with the driving stress at the centerline

$$\tau_{dx}(0) = -\rho g H_o \frac{\partial h}{\partial x}. \quad (4.34)$$

Also shown in the upper panels is the velocity at the glacier surface, normalized with the surface velocity at the centerline as predicted by the lamellar flow theory with $n = 3$ and no basal sliding:

$$U_d(0) = \frac{1}{2} A H_o \tau_{dx}^3(0). \quad (4.35)$$

The other panels in the figures show the normalized component of velocity in the direction of flow, the normalized vertical shear stress, and the normalized lateral shear stress.

The effect of the width-to-depth ratio is perhaps best seen in the panels showing the normalized velocity. For the glacier in a relatively narrow basin ([Figure 4.5](#)),

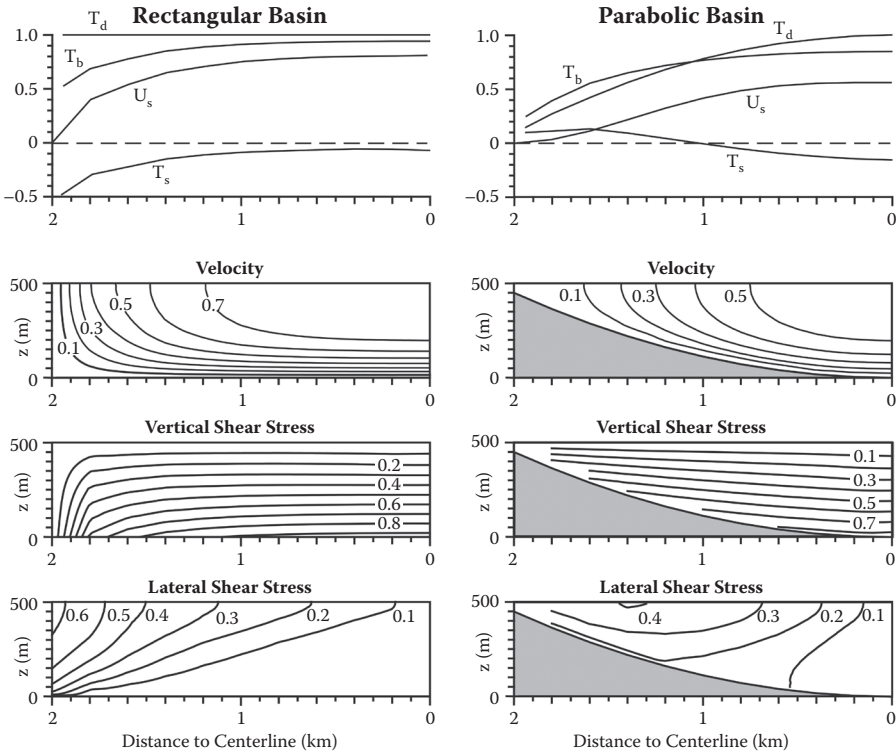


FIGURE 4.5 Effect of lateral drag on a shallow glacier ($W/H_0 = 4$) in a rectangular basin (panels on the left) and parabolic basin (panels on the right; shading indicates bedrock). The upper panels show driving stress (T_d), lateral drag (T_s), and basal drag (T_b) nondimensionalized with the driving stress at the center, as well as the surface velocity (U_s) nondimensionalized with the surface velocity at the centerline as predicted by the lamellar-flow theory (equation (4.24)). The other panels show cross-sectional views of the nondimensionalized velocity, vertical shear stress, and lateral shear stress.

calculated velocities are smaller than for the glacier in the wide valley (Figure 4.6). The reason for this is that lateral drag provides more resistance to flow when the glacier basin is narrow. Consequently, drag at the glacier base is smaller than the driving stress. Near the glacier center, where the velocity may be calculated from the lamellar flow theory with the driving stress replaced by basal drag, the surface velocity is therefore less than it would be in the absence of lateral drag.

There is a marked difference between the flow through a rectangular cross-section and the flow through a parabolic basin (Nye, 1965c). This difference is most clearly shown in Figure 4.5, representing relatively narrow glaciers. For the rectangular basin, the curve of the surface velocity is always convex, implying that lateral drag (being proportional to the second cross-flow derivative of the velocity) is always negative, that is, opposing the flow of the glacier. For the parabolic basin, the curve of the surface velocity has an inflection point (in the case of Figure 4.5

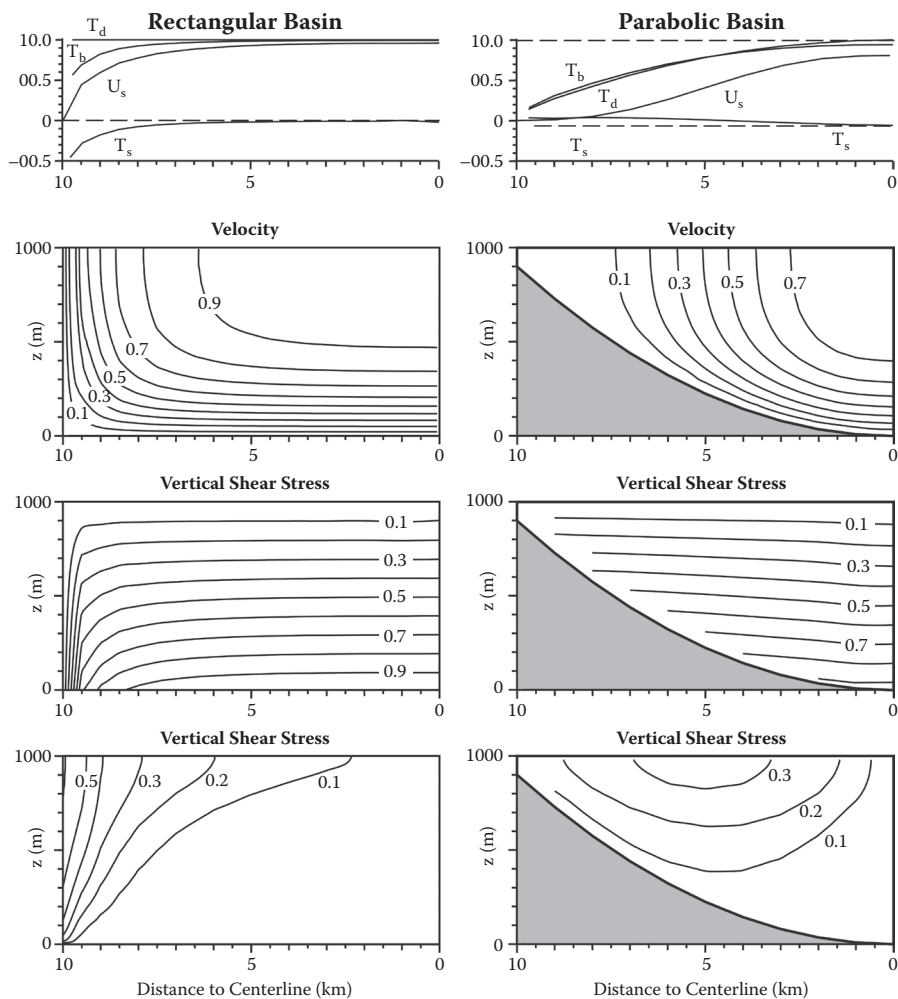


FIGURE 4.6 As Figure 4.5, for $W/H_0 = 10$.

at $y = 1$ km), caused by the decreasing driving stress toward the margins (although the surface slope is taken constant across the width of the glacier, the ice thickness, and hence the driving stress, decreases away from the centerline). The concave curvature of the velocity curve indicates positive lateral drag near the margins; in the center, where this curvature is convex, lateral drag is negative. This means that the center ice is dragging the margin ice along, and a region exists near the margins where basal drag exceeds the local driving stress.

All examples show that, at the centerline, the vertical shear stress, R_{xz} , increases approximately linearly with depth, and that lamellar flow theory may be applied to the central parts to calculate the surface velocity. How well this linear dependency applies to the main body of the glacier depends on the width-to-height ratio, W/H_0 . To account quantitatively for the effect of the valley walls on the glacier flow, Nye

TABLE 4.1
Shape Factors Corresponding to the Examples in Figures 4.5 and 4.6

	Shape Factor from Centerline Surface Velocity	Shape Factor from Width-Averaged Force Balance
Rectangular basin, W/H _o = 4	0.93	0.87
Rectangular basin, W/H _o = 10	0.99	0.96
Parabolic basin, W/H _o = 10	0.83	0.98
Parabolic basin, W/H _o = 10	0.93	0.99

(1965c) introduced the *shape factor*. This factor, commonly denoted by f , represents the fraction of driving stress that is supported by basal drag, the remainder of resistance being due to lateral drag. That is

$$\tau_{bx} = f \tau_{dx} \tag{4.36}$$

The shape factor can be calculated as that needed to produce the correct surface velocity at the centerline if lamellar flow is assumed, or it can be calculated from force balance for the entire width of the glacier. Both methods yield results that differ by about 10% to 20%, depending on the shape of the glacier basin. The reason for this is that using the centerline velocity to calculate the shape factor yields a local value applicable to the centerline only. If, on the other hand, the large-scale balance of forces is invoked to determine the shape factor, a width-averaged value of f is found. Because in general, local basal drag does not support the same fraction of the local driving stress across the width of the glacier (as shown in the upper panels of Figures 4.5 and 4.6), a difference between both values may be expected. Shape factors calculated using both methods for the examples shown in Figures 4.5 and 4.6 are given in Table 4.1. Shape factors for some other geometries were determined by Nye (1965c) and are given in Table 4.2.

In the model of Nye (1965c), as well as in the model described above, the ice is taken to flow by internal deformation only, with no basal slip. However, observations conducted on Athabasca Glacier in Alberta, Canada, indicate that basal sliding accounts for about 80% of the surface velocity near the center of that glacier. Toward the margins, the sliding velocity decreases (Raymond, 1971). This result prompted Reynaud (1973) and Harbor (1992) to incorporate basal sliding into their numerical models for flow in a valley glacier cross-section. To obtain reasonable agreement between model predictions and the transverse velocity profile derived from the measurements given in Raymond (1971), in particular the observed small sliding velocities near the margin, Harbor (1992) had to make the assumption that the friction increases toward the margin. However, as pointed out by Harbor (1992), there are not enough constraining measurements to validate this assumption.

TABLE 4.2

Shape Factor from Centerline Surface Velocity for Various Cross-Sectional Basins, Calculated by Nye (1965c)

W/H_0	Rectangular Basin	Ellipsoidal Basin	Parabolic Basin
0	0	0	0
1/4	—	0.134	—
1/3	0.204	0.185	—
1/2	0.313	0.281	—
1	0.558	0.500	0.445
2	0.789	0.709	0.646
3	0.884	0.799	0.746
4	—	0.849	0.806
∞	1.000	1.000	1.000

4.4 GLACIER FLOW CONTROLLED BY LATERAL DRAG

Lateral drag originates at the margins, where glacier ice moves past rock walls or, as in the case of ice streams, past nearly stagnant ice. Because most glaciers are comparatively shallow with respect to their width, with ice thicknesses less than about 2 km, the area over which lateral drag acts (the vertical sides of the glacier) is limited. This means that there is a practical upper limit to how much driving stress can be supported by lateral drag. In contrast, basal drag acts over the full width of the glacier and can therefore support a larger driving stress. This difference between both sources of flow resistance can be quantified by considering the force budget averaged over the width of the glacier.

Making the assumption that the lateral shear stress, R_{xy} , is constant with depth, and neglecting gradients in longitudinal stress, the force-balance equation (3.22) reduces to

$$\tau_{dx} = \tau_{bx} - \frac{\partial}{\partial y}(HR_{xy}). \quad (4.37)$$

The lateral resistance averaged over the half width, W , is

$$\begin{aligned} -\frac{\partial}{\partial y}(HR_{xy}) &= -\frac{1}{W} \int_{-W}^0 \frac{\partial}{\partial y}(HR_{xy}) dy = \\ &= -\frac{1}{W}(HR_{xy}(0) - HR_{xy}(-W)). \end{aligned} \quad (4.38)$$

Flow through the cross-section is symmetric around the centerline ($y = 0$) so that the shear stress, R_{xy} , is zero there. Denoting the lateral shear stress at the margin ($y = -W$)

by τ_s , and the thickness at the margin by H_w , the lateral resistance on a section of glacier of unit width is

$$F_s = \frac{H_w \tau_s}{W}, \quad (4.39)$$

and the width-averaged force-balance equation becomes

$$\bar{\tau}_{dx} = \bar{\tau}_{bx} + \frac{H_w \tau_s}{W}, \quad (4.40)$$

with an overbar denoting a width-averaged value.

To estimate the potential importance of lateral drag, a value for the shear stress at the margins, τ_s , is needed. Ice is often considered a plastic material with a yield stress of about 100–200 kPa (Section 5.1). This observation is based on the rather narrow range of values of basal drag determined for various glaciers (as shown in Figure 4.3). It seems reasonable therefore to use a similar upper limit to the lateral shear stress at the margins. For a typical mountain glacier such as Columbia Glacier, with a half width of about 3 km and a marginal thickness of about 200 m, a shear stress at the margins of 200 kPa can support only 13 kPa of driving stress. Basal drag comparable to the yield stress, on the other hand, can support 200 kPa of driving stress. With driving stresses typically on the order of 50–200 kPa, the practical upper limit to resistance offered by lateral drag limits the role of sidewall friction to opposing about 25% or less of the driving stress (as also indicated by the shape factors given in Table 4.2). A notable exception to this may be the West Antarctic ice streams, where high speeds (up to 800 m/yr on Whillans Ice Stream; Whillans and Van der Veen, 1993b) are achieved in spite of unusually small driving stresses (about 15 kPa; Alley and Whillans, 1991). This combination of high speed, and associated lateral shear at the margins, with small surface slope allows for the possibility that the flow of these ice streams is controlled entirely by lateral drag. Whillans and Van der Veen (1997) present several arguments in favor of ice stream flow controlled by lateral drag. Another instance where lateral drag opposes a significant part of the driving stress is on the lower reach of Jakobshavn Isbræ, on the west coast of Greenland. The fast-moving part of this outlet glacier is very narrow (*ca.* 6 km), and the ice thickness at the shear margin is about 1500 m. Because of this geometry, lateral drag supports in excess of 200 kPa of driving stress just upglacier of the grounding line (Van der Veen et al., 2011).

With lateral drag providing the sole resistance to flow, the force-balance equation (4.37) reduces to

$$\tau_{dx} = -\frac{\partial}{\partial x}(H R_{xy}). \quad (4.41)$$

Any (small) residual basal drag may be accounted for by defining an “effective” driving stress

$$\hat{\tau}_{dx} = \tau_{dx} - \tau_{bx}. \quad (4.42)$$

Taking the driving stress (or effective driving stress) and ice thickness constant across the width of the glacier, it follows from the balance equation (4.41) that the shear stress, R_{xy} , varies linearly across the glacier and

$$R_{xy}(y) = ay + b. \quad (4.43)$$

At the centerline ($y = 0$) this shear stress is zero, so that $b = 0$. As above, lateral drag at the margins is denoted by $+\tau_s$ ($y = -W$) and $-\tau_s$ ($y = +W$). From the balance equation (4.40) it follows that

$$\tau_s = \frac{W}{H} \hat{\tau}_{dx}, \quad (4.44)$$

giving the shear stress across the glacier

$$R_{xy}(y) = -\frac{y}{H} \hat{\tau}_{dx}. \quad (4.45)$$

The transverse profile of velocity is found by invoking the constitutive relation linking stresses to strain rates. In the present model the only nonzero strain rate is the rate of lateral shearing

$$\dot{\epsilon}_{xy} = \frac{1}{2} \frac{\partial U}{\partial y}. \quad (4.46)$$

The flow law then reduces to

$$R_{xy} = B \left(\frac{1}{2} \frac{\partial U}{\partial y} \right)^{1/n}, \quad (4.47)$$

or

$$\frac{\partial U}{\partial y} = 2 \left(\frac{R_{xy}}{B} \right)^n. \quad (4.48)$$

Substituting expression (4.47) for the shear stress, and integrating with respect to y , gives

$$U(y) = -\frac{2}{n+1} \left(\frac{\hat{\tau}_{dx}}{BH} \right)^n + C. \quad (4.49)$$

The integration constant, C , follows from the no-slip boundary condition at both margins:

$$C = \frac{2}{n+1} \left(\frac{\hat{\tau}_{dx}}{BH} \right)^n W^{n+1}. \quad (4.50)$$

The transverse velocity profile can now be written as

$$U(y) = U(0) \left(1 - \left(\frac{y}{W} \right)^{n+1} \right), \quad (4.51)$$

with the centerline velocity given by

$$U(0) = \frac{2}{n+1} \left(\frac{\hat{\tau}_{dx}}{BH} \right)^n W^{n+1}. \quad (4.52)$$

These expressions for the transverse profile of velocity are very similar to equations (4.23) and (4.24) derived for lamellar flow. This is because both models are essentially the same with the controlling shear stress, R_{xz} or R_{xy} , respectively, decreasing linearly from the site of friction (the glacier bed, or the glacier margin) to zero at either the glacier surface or its centerline. However, because glaciers are mostly shallow, with relatively large width compared with the depth, the lateral-control model may lead to centerline velocities that are orders of magnitudes larger than the surface velocity predicted by the lamellar-flow theory.

4.5 ICE-SHELF SPREADING

In the models discussed so far in this chapter, gradients in longitudinal stress have been neglected as a source of flow resistance, and the driving stress was assumed to be balanced by drag at the glacier bed and/or lateral drag. However, on floating ice shelves, basal drag is obviously zero, and lateral drag may be small if the shelf has formed in a wide embayment or is floating freely. In that case, all resistance to flow is associated with longitudinal stresses. The resulting flow solution was first derived by Weertman (1957b). Note that in the Weertman model, an ice shelf of constant thickness is considered. This is an unrealistic situation as it would imply a zero surface slope and thus no driving stress. The following derivation does not make any assumption about the geometry of the ice shelf, other than that the ice is in hydrostatic equilibrium with the sea water, and arrives at the same result as did Weertman (1957b).

For a free-floating ice shelf, the force-balance equation (3.22) reduces to a balance between driving stress and gradients in longitudinal stress, such that

$$\tau_{dx} = - \frac{\partial}{\partial x} \int_{h-H}^h R_{xx} \, dz, \quad (4.53)$$

where h represents the surface elevation and H the thickness of the ice shelf. Neglecting the depth variation in the longitudinal resistive stress, R_{xx} (as seems reasonable because vertical shear in an ice shelf is negligible; Sanderson and

Doake, 1979), and using equation (3.21) for the definition of the driving stress, the balance equation simplifies to

$$\rho g H \frac{\partial h}{\partial x} = \frac{\partial}{\partial x} (H R_{xx}). \quad (4.54)$$

This equation can be solved for the resistive stress, R_{xx} , by eliminating the surface elevation, h . Because ice shelves are floating in sea water, the height of the ice surface above sea level follows from hydrostatic equilibrium

$$h = \left(1 - \frac{\rho}{\rho_w}\right) H, \quad (4.55)$$

where ρ_w represents the density of sea water and ρ the density of ice. Substituting this expression for h in the balance equation (4.54) gives

$$\frac{1}{2} \rho g \left(1 - \frac{\rho}{\rho_w}\right) \frac{\partial H^2}{\partial x} = \frac{\partial}{\partial x} (H R_{xx}). \quad (4.56)$$

Integrating with respect to x gives the longitudinal resistive stress

$$R_{xx} = \frac{1}{2} \rho g \left(1 - \frac{\rho}{\rho_w}\right) H + C. \quad (4.57)$$

For an (imaginary) ice shelf of zero thickness, the resistive stress, R_{xx} , must be zero so the integration constant, C , must be zero and

$$R_{xx} = \frac{1}{2} \rho g \left(1 - \frac{\rho}{\rho_w}\right) H. \quad (4.58)$$

The next step is to derive an expression for the horizontal strain rates in the ice shelf. The rate of longitudinal spreading, or creep rate, can be found by invoking the constitutive relation. Bridging effects (discussed in Section 3.4) are zero because the weight of the shelf ice is locally supported by the sea water. Following Thomas (1973), the rate of transverse spreading and lateral shearing are linked to the along-flow creep rate as

$$\dot{\epsilon}_{yy} = \alpha \dot{\epsilon}_{xx}, \quad (4.59)$$

$$\dot{\epsilon}_{xy} = \beta \dot{\epsilon}_{xx}, \quad (4.60)$$

where α and β are functions of horizontal position (depending on shelf geometry) but constant over the ice thickness. The effective strain rate is then

$$\dot{\epsilon}_e^2 = (1 + \alpha + \alpha^2 + \beta^2) \dot{\epsilon}_{xx}^2, \quad (4.61)$$

and inverting the flow law gives

$$\dot{\epsilon}_{xx} = \theta \left(\frac{R_{xx}}{B} \right)^n, \quad (4.62)$$

with

$$\theta = \frac{(1 + \alpha + \alpha^2 + \beta^2)^{(n-1)/2}}{(2 + \alpha)^n}. \quad (4.63)$$

For an ice shelf that is spreading only in the direction of flow (that is, an ice shelf in a parallel-sided bay, with zero or small sidewall friction), $\alpha = \beta = 0$. Substituting expression (4.58) for the longitudinal resistive stress into equation (4.62) gives the expression for the creep rate as derived by Weertman (1957b):

$$\dot{\epsilon}_{xx} = \left[\frac{\rho g}{4B} \left(1 - \frac{\rho}{\rho_w} \right) \right]^n H^n. \quad (4.64)$$

If the ice shelf is floating freely, spreading may be expected to be uniform in both horizontal directions ($\alpha = 1$) with creep rates

$$\dot{\epsilon}_{xx} = \dot{\epsilon}_{yy} = 3^{-(n+1)/2} \left[\frac{\rho g}{4B} \left(1 - \frac{\rho}{\rho_w} \right) \right]^n H^n. \quad (4.65)$$

Few of the Antarctic ice shelves are spreading freely, and most have formed in embayments, with lateral drag providing additional resistance to flow. Thomas (1973) includes lateral drag in his model for ice-shelf spreading by making the assumption that the lateral shear stress, R_{xy} , is constant throughout the entire ice thickness and varies linearly in the transverse direction:

$$R_{xy}(y) = -\frac{y}{W} \tau_s, \quad (4.66)$$

with W representing the half-width of the ice shelf and τ_s the shear stress at the margins (as in Section 4.4). By adopting this transverse profile for R_{xy} , the assumption is made that resistance from lateral drag is equally important across the entire width of the ice shelf. Adding lateral drag to the balance equation (4.53) gives

$$\tau_{dx} = -\frac{\partial}{\partial x}(HR_{xx}) + \frac{H\tau_s}{W}, \quad (4.67)$$

or

$$\frac{\partial}{\partial x}(HR_{xx}) = \frac{1}{2} \rho g \left(1 - \frac{\rho}{\rho_w} \right) \frac{\partial H^2}{\partial x} - \frac{H\tau_s}{W}. \quad (4.68)$$

Integrating this expression from the ice-shelf front ($x = L$) to some distance $L - x$ upglacier, yields

$$\begin{aligned} HR_{xx}(L) - HR_{xx}(L - x) &= \\ &= \frac{1}{2} \rho g \left(1 - \frac{\rho}{\rho_w} \right) [H^2(L) - H^2(L - x)] - \int_L^{L-x} \frac{H\tau_s}{W} d\bar{x}. \end{aligned} \quad (4.69)$$

At the shelf front, R_{xx} may be calculated from expression (4.58), and the longitudinal resistive stress on the ice shelf is

$$R_{xx}(x) = \frac{1}{2} \rho g \left(1 - \frac{\rho}{\rho_w} \right) H - \frac{1}{H} \int_x^L \frac{H\tau_s}{W} d\bar{x}, \quad (4.70)$$

with the x -axis directed toward the terminus (so that $x < L$ on the ice shelf).

Again, the spreading rate is found by inverting the constitutive relation. For brevity, the creep rate is written as

$$\dot{\epsilon}_{xx} = \theta \left(\frac{R_{xx}^{(0)} - \sigma_b}{B} \right)^n, \quad (4.71)$$

in which θ is defined as above (equation (4.63)). In this expression, $R_{xx}^{(0)}$ represents the stretching stress for a free-floating ice shelf given by equation (4.58), while σ_b represents a “back pressure” arising from lateral shear (Thomas and Bentley, 1978; MacAyeal, 1987). At any point on the ice shelf, this back pressure is defined as the downglacier integrated resistance associated with lateral drag:

$$\sigma_b(x) = \frac{1}{H} \int_x^L \frac{H\tau_s}{W} d\bar{x}. \quad (4.72)$$

Thus, the more important lateral drag, the larger the back pressure. The result of this additional resistance from lateral drag is a reduced spreading rate when compared with that of a free-floating ice shelf.

The physical significance of the back pressure as introduced above may be somewhat difficult to understand because the above definition involves comparing a real ice shelf to an imaginary “Weertman-type” ice shelf that is spreading freely. Recall, however, that the Weertman solution is derived from the assumption that gradients in longitudinal stress balance the driving stress and integrating the resulting force-balance equation in the direction of flow. Therefore, at any point on the ice shelf, $R_{xx}^{(0)}$ represents the total driving force per unit width (that is, the integrated driving stress) acting on the section of shelf extending beyond a point

x to the shelf front at $x = L$. Thus, comparing the back pressure with the resistive stress that one would find on a free-floating ice shelf is equivalent to comparing the net resistance to flow associated with lateral drag along this stretch of the ice shelf with the net driving force. If both are the same, all flow resistance is due to lateral drag. On the other hand, if the back pressure is zero, the resistance to flow arises entirely from gradients in longitudinal stress (as for a free-floating ice shelf). In other words, the backstress at any point on an ice shelf represents the fraction of the total driving force acting on the section of ice shelf extending from that point to the calving front, that is, supported by lateral drag and/or basal drag acting on that section.

To illustrate the procedure for estimating back stress, consider a flowline extending from the grounding line of Whillans Ice Stream to the front of the Ross Ice Shelf. At the survey stations on the ice shelf shown in Figure 4.7, the three surface strain rates were determined from the deformation of small strain rosettes (tabulated in Thomas et al., 1984; reproduced here in Table 4.3). Although these strain rates represent local values that may not be entirely representative of larger areas, the errors are sufficiently small to favor using these data rather than large-scale averages

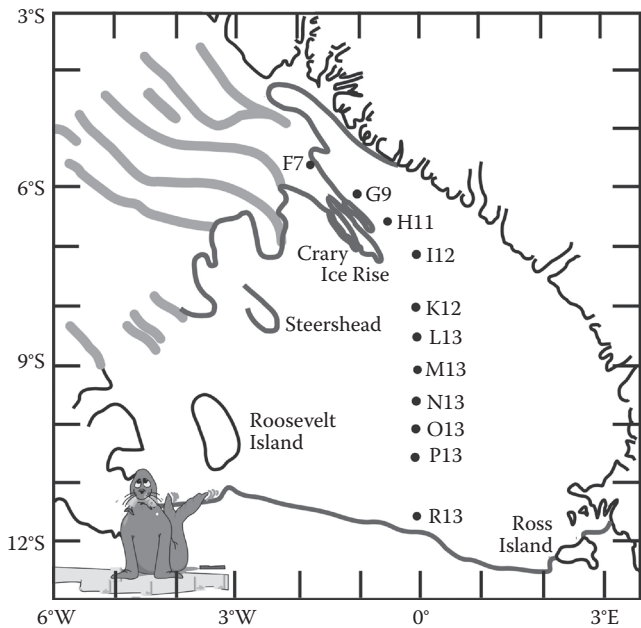


FIGURE 4.7 Location of the stations on the flowline used to calculate back stress on the Ross Ice Shelf. Marginal numbers are grid coordinates, with the Greenwich meridian as grid longitude 0°, and the South Pole at grid latitude 0° (Bentley et al., 1979); 1° in either direction equals 111 km. Light shading indicates lateral shear margins of the ice streams; dark shading represent the grounding line and the ice-shelf front. (From Whillans, I. M., and C. J. van der Veen, *J. Glaciol.*, 39, 483–490, 1993. Reprinted from the *Journal of Glaciology* with permission of the International Glaciological Society and the authors.)

TABLE 4.3
Data Used to Estimate the Role of Gradients in Longitudinal Stress on the Ross Ice Shelf

Station	x (km)	H (m)	U (m/yr)	$\dot{\alpha}_x$	$\dot{\alpha}_y$	$\dot{\alpha}_y$
				(10^{-5} yr^{-1})	(10^{-5} yr^{-1})	(10^{-5} yr^{-1})
F17	300.2	760	530	-11.2 ± 15.1	154.2 ± 6.7	43.6 ± 4.1
G9	405.0	620	450	-69.0 ± 2.5	48.0 ± 2.5	-81.7 ± 1.7
H11	481.2	605	432	-1.8 ± 4.9	76.8 ± 4.9	-9.8 ± 0.9
I12	562.0	523	501	49.8 ± 2.9	72.2 ± 5.3	20.0 ± 3.3
K12	664.4	400	547	56.1 ± 1.0	14.9 ± 3.5	18.2 ± 1.4
L13	721.5	365	582	72.3 ± 1.0	1.7 ± 1.0	-16.6 ± 0.3
M13	781.3	360	616	111.4 ± 12.6	-35.4 ± 8.7	26.4 ± 2.7
N13	836.2	360	705	147.5 ± 1.9	-72.5 ± 1.0	-38.3 ± 0.4
O13	893.4	345	815	167.9 ± 5.5	-128.9 ± 3.7	-106.2 ± 2.1
P13	942.2	320	893	134.4 ± 3.7	-50.4 ± 1.9	-63.3 ± 1.3
R13	1057.7	295	998	74.9 ± 1.0	56.2 ± 3.6	-6.7 ± 1.2

Source: Based on data from Thomas, R. H., in *The Ross Ice Shelf: Glaciology and Geophysics*, American Geophysical Union, Antarctic Research Series, Washington, DC, 42, 21–53, 1984.

Note: Strain Rates are defined with respect to a (local) flow-following coordinate system, with x in the direction of flow, and y perpendicular to it.

calculated from velocity gradients. At each station, $R_{xx}^{(0)}$ is estimated from the ice thickness using equation (4.58). Rewriting equation (4.71) as

$$\sigma_b = R_{xx}^{(0)} - B \left(\frac{\dot{\epsilon}_{xx}}{\theta} \right)^{1/n}, \tag{4.73}$$

the back pressure can then be calculated from measured strain rates.

The calculated back pressure is shown in the upper panel of Figure 4.8. As expected, σ_b increases steadily toward the grounding line (because σ_b represents lateral drag integrated from the ice front toward the interior, and lateral drag cannot be negative). This means that lateral drag is important along the entire ice shelf; if at some site lateral drag would be zero, the curve of σ_b would show a horizontal plateau. Comparison with the curve of $R_{xx}^{(0)}$ in the lower panel of Figure 4.8 shows that both are very similar, indicating that lateral drag is the most important source of flow resistance. $R_{xx}^{(0)}$ as given by equation (4.58) represents the driving stress integrated from the ice-shelf front in the upstream direction. If gradients in longitudinal stress were to be dominant, the longitudinal resistive stress, R_{xx} , calculated from the strain rates (also shown in the lower panel of Figure 4.8), would be (almost) the same as $R_{xx}^{(0)}$. The fact that both curves in the lower panel of Figure 4.8 are so different indicates that gradients in longitudinal stress are unimportant along this flowline.

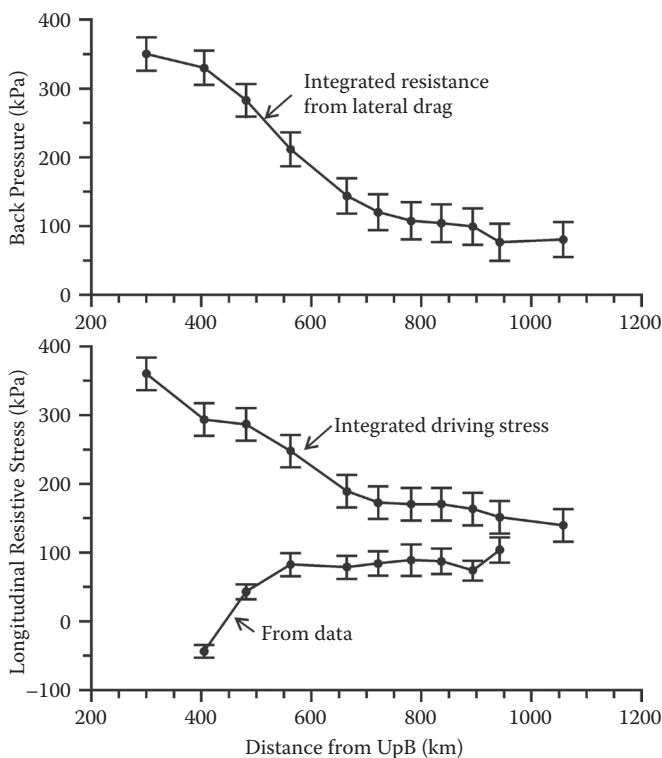


FIGURE 4.8 Calculated back pressure, σ_b , at the stations on the Ross Ice Shelf (upper panel). The lower panel shows the longitudinal resistive stress, R_{xx} , as calculated from equation (4.58) (the value predicted for a free-spreading ice shelf, corresponding to the integrated driving stress), as well as the values calculated from measured strain rates.

4.6 ALONG-FLOW VARIATIONS IN GLACIER FLOW

An important problem in glaciology is the transfer of flow or topographic irregularities at the glacier base to the surface. This topic is of importance because processes at the glacier base may be controlling the mechanics and motion of the glacier and lead to surface undulations or small-scale variations in surface velocity. Direct observation of basal processes is often impossible or very expensive and labor intensive and limited to individual boreholes reaching the glacier bed. The glacier surface, on the other hand, is more readily accessible for measurements, and surface observations are often used to infer conditions at the glacier bed (for example, Thorsteinsson et al., 2003). The difficulty with such procedures is that basal perturbations propagate upward but do so with decreasing amplitude so that, generally, the surface expression is much smaller than the causal bed variations. Inverting this glacier filter to infer basal conditions from surface measurements could lead to calculated patterns of basal drag being dominated by small-scale surface features. Thus, what is needed is an analytical framework that describes the surface response to small

amplitude variations in bed topography or basal sliding. This has been discussed many times before (for example, Balise and Raymond, 1985; Balise, 1988; Budd, 1970a, b; Gudmundsson, 1997, 2003, 2008; Hutter, 1981, 1983, Chapter 4; Hutter et al., 1981; Kamb, 1970; Nye, 1969a; Whillans and Johnsen, 1983). Generally, simplifying assumptions are introduced such as linear viscosity, small-amplitude basal variations that allow for a perturbation analysis, or simplified form of the sliding relation linking basal drag to sliding speed. Nevertheless, the analytical treatment becomes quite complex and involved.

The main obstacle to finding analytical solutions that describe glacier flow is the nonlinearity of the constitutive relation (Section 2.2). For this reason, many earlier authors adopted a linear ice rheology in which a particular component of stress depends only on the corresponding component of strain rate (rather than on all other strain rates through the effective strain rate, as in Glen's flow law). The effective viscosity is either taken constant throughout the ice thickness or varies in a prescribed way with depth. The main advantage of a linear rheology is that the stress and velocity solutions may be split in an average and a perturbation component. Doing so leads to a biharmonic solution for the perturbation velocity field, which describes how basal variations are transferred to the glacier surface. Below, this procedure is discussed, based mainly on the analyses of Whillans and Johnsen (1983) and Balise and Raymond (1985). Because the mathematics involved tend to become rather lengthy, the solution method is emphasized more than the analytical procedures.

The geometry is shown in Figure 4.9. Plane flow in the (x, z) plane is considered, with the x -axis along the mean surface of the glacier and the z -axis perpendicular to the x -axis and directed upward. The mean bed is parallel to the glacier surface, as in the plane-slab model.

Adopting a linear rheology allows partitioning of stress and velocity in an average and a perturbation component (denoted by an overbar and a tilde, respectively). Note that the perturbations need not be small compared with the averages. For full stresses, this division gives

$$\sigma_{ij} = \bar{\sigma}_{ij} + \tilde{\sigma}_{ij}, \quad (4.74)$$

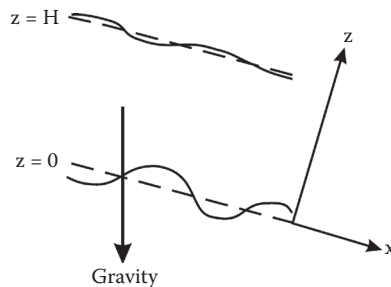


FIGURE 4.9 Geometry of the model for describing along-flow variations in glacier flow. Undulations in the basal and surface topography are exaggerated for clarity.

with the average stress defined as

$$\bar{\sigma}_{ij} = \frac{1}{L} \int_{x-L/2}^{x+L/2} \sigma_{ij} \, dx. \quad (4.75)$$

Here, L is the averaging length, which must be much larger than the ice thickness.

For the chosen system, the component of gravity in the x -direction is $g_x = -\rho g \sin \alpha$, and that in the z -direction is $g_z = -\rho g \cos \alpha$, where ρ represents the density of the ice, g the gravitational acceleration, and α the mean surface (and basal) slope. The equivalent forms of the balance equations (3.8) and (3.10) are then

$$\frac{\partial \sigma_{xx}}{\partial x} + \frac{\partial \sigma_{xz}}{\partial z} = \rho g \sin \alpha, \quad (4.76)$$

$$\frac{\partial \sigma_{xz}}{\partial x} + \frac{\partial \sigma_{zz}}{\partial z} = \rho g \cos \alpha. \quad (4.77)$$

Averaging these equations over the distance L gives

$$\frac{\partial \bar{\sigma}_{xx}}{\partial x} + \frac{\partial \bar{\sigma}_{xz}}{\partial z} = \rho g \sin \alpha, \quad (4.78)$$

$$\frac{\partial \bar{\sigma}_{xz}}{\partial x} + \frac{\partial \bar{\sigma}_{zz}}{\partial z} = \rho g \cos \alpha. \quad (4.79)$$

Subtracting the averaged equations (4.78) and (4.79) from the full equations (4.76) and (4.77), respectively, gives the balance equations for the stress perturbations

$$\frac{\partial \tilde{\sigma}_{xx}}{\partial x} + \frac{\partial \tilde{\sigma}_{xz}}{\partial z} = 0, \quad (4.80)$$

$$\frac{\partial \tilde{\sigma}_{xz}}{\partial x} + \frac{\partial \tilde{\sigma}_{zz}}{\partial z} = 0. \quad (4.81)$$

These equations show that the gravitational body forces are associated with the average stresses. The perturbation solution is independent of the gravitational forces, except where these forces enter into the boundary conditions (Whillans and Johnsen, 1983).

The next step is to derive the biharmonic perturbation equation from which the perturbation velocities can be calculated. First, differentiating equation (4.80) with respect to z and equation (4.81) with respect to x , and subtracting the two resulting equations, gives

$$\frac{\partial^2 \tilde{\sigma}_{xz}}{\partial z^2} - \frac{\partial^2 \tilde{\sigma}_{xz}}{\partial x^2} + \frac{\partial^2}{\partial x \partial z} (\tilde{\sigma}_{xx} - \tilde{\sigma}_{zz}) = 0. \quad (4.82)$$

Because strain rates are linked to stress deviators, this equation, containing perturbations of the full stress components, needs to be rewritten in terms of perturbation stress deviators. For plane flow, the spherical stress equals $(\sigma_{xx} + \sigma_{zz})/2$, and the perturbation component of the normal stress deviator is

$$\begin{aligned}\tilde{\tau}_{xx} &= \tilde{\sigma}_{xx} - \frac{1}{2}(\tilde{\sigma}_{xx} + \tilde{\sigma}_{zz}) = \\ &= \frac{1}{2}(\tilde{\sigma}_{xx} - \tilde{\sigma}_{zz}).\end{aligned}\quad (4.83)$$

With the deviatoric shear stress equal to the full shear stress, equation (4.82) can also be written as

$$\frac{\partial^2 \tilde{\tau}_{xz}}{\partial z^2} - \frac{\partial^2 \tilde{\tau}_{xz}}{\partial x^2} + 2 \frac{\partial^2 \tilde{\tau}_{xx}}{\partial x \partial z} = 0. \quad (4.84)$$

The ice is assumed to obey a linear constitutive relation and

$$\tau_{ij} = 2\eta \dot{\epsilon}_{ij}, \quad (4.85)$$

where η represents the effective viscosity of the ice, taken constant here. Using this relation between stress and strain rate, and the definition of strain rates (Section 1.2), allows equation (4.84) to be written in terms of the perturbation velocities:

$$2\eta \frac{\partial^2}{\partial z^2} \left[\frac{1}{2} \left(\frac{\partial \tilde{u}}{\partial z} + \frac{\partial \tilde{w}}{\partial x} \right) \right] - 2\eta \frac{\partial^2}{\partial x^2} \left[\frac{1}{2} \left(\frac{\partial \tilde{u}}{\partial z} + \frac{\partial \tilde{w}}{\partial x} \right) \right] + 4\eta \frac{\partial^2}{\partial x \partial z} \left[\frac{\partial \tilde{u}}{\partial x} \right] = 0. \quad (4.86)$$

It is now convenient to introduce a stream function, Ψ , as

$$\begin{aligned}\tilde{u} &= \frac{\partial \Psi}{\partial z}, \\ \tilde{w} &= -\frac{\partial \Psi}{\partial x}.\end{aligned}\quad (4.87)$$

By defining the stream function this way, the incompressibility condition (1.39) is always satisfied. Replacing velocities in equation (4.86) by derivatives of the stream function gives

$$\frac{\partial^4 \Psi}{\partial x^4} + \frac{\partial^4 \Psi}{\partial z^4} + 2 \frac{\partial^4 \Psi}{\partial x^2 \partial z^2} = 0. \quad (4.88)$$

This equation does not contain the effective viscosity, η , and the perturbation velocities are independent of the stiffness of the glacier ice. The perturbation stresses are, of course, dependent on the effective viscosity through the flow law (4.85).

The perturbation solution can now be found by solving the biharmonic equation (4.88) for the stream function, Ψ . For example, Whillans and Johnsen (1983) adopt a solution that is periodic in x and varies exponentially with depth

$$\begin{aligned}\Psi = & \left[(a_1 + a_2 z) e^{\omega z} + (a_3 + a_4 z) e^{-\omega z} \right] \sin \omega x + \\ & + \left[(a_5 + a_6 z) e^{\omega z} + (a_7 + a_8 z) e^{-\omega z} \right] \cos \omega x.\end{aligned}\quad (4.89)$$

The eight constants a_i are to be determined from the boundary conditions, including those associated with variations in the surface and basal topography. To avoid lengthy arithmetic, the example of transfer of basal sliding variations to the surface (Balise and Raymond, 1985; Balise, 1988) is considered next, neglecting variations in the surface and basal topography. This simplifies the general form of the stream function and reduces the number of required boundary conditions to four. The more elaborate procedure followed by Whillans and Johnsen (1983) is essentially the same as that discussed below.

Balise and Raymond (1985) and Balise (1988) investigate the transfer of basal velocity anomalies to the surface of a glacier that is approximated as a planar parallel-sided slab of constant thickness, H . Using the Fourier transform of the biharmonic equation (4.88), surface velocities can be found for any perturbation in basal velocity. To illustrate the solution method and the basic properties of the transfer function, the example of a harmonic surface-parallel basal velocity anomaly is discussed here, following Balise (1988). The formulas given in Balise (1988) and below differ from those in Balise and Raymond (1985) because the latter authors use a coordinate system in which the z -axis is directed downward. Here, as in Balise (1988), the z -axis is positive upward.

The perturbation velocity parallel to the glacier bed is taken to be periodic in the flow direction as

$$\tilde{u}_b(x) = U_b \sin \omega x, \quad (4.90)$$

where U_b represents the amplitude of the basal perturbation. The perturbation velocity perpendicular to the bed is set to zero:

$$\tilde{w}_b(x) = 0. \quad (4.91)$$

The basal boundary conditions compatible with these basal velocity perturbations follow immediately from definition (4.87) of the stream function:

$$\frac{\partial \Psi}{\partial z} = U_b \sin \omega x, \quad (z = 0) \quad (4.92)$$

and

$$\frac{\partial \Psi}{\partial x} = 0. \quad (z = 0). \quad (4.93)$$

Variations in the surface and bed topography are neglected and the general solution adopted by Whillans and Johnsen (1983) may be simplified somewhat by omitting the cosine-term on the right-hand side of equation (4.89). That is

$$\Psi(x, z) = U_b \left[(a_1 + a_2 z) e^{\omega z} + (a_3 + a_4 z) e^{-\omega z} \right] \sin \omega x. \quad (4.94)$$

This expression contains four constants to be determined. Thus, in addition to the two boundary conditions (4.92) and (4.93) applying to the glacier base, two more boundary conditions are needed. These follow from the condition that the glacier surface must be stress free.

Because the x -axis is chosen parallel to the glacier surface, the shear stress at the surface must be zero and

$$\tilde{\tau}_{xz}(x, H) = 0. \quad (4.95)$$

Using the linear constitutive relation (4.85), this condition is equivalent to

$$\frac{\partial \tilde{u}}{\partial z} + \frac{\partial \tilde{w}}{\partial x} = 0, \quad (z = H) \quad (4.96)$$

or in terms of the stream function,

$$\frac{\partial^2 \Psi}{\partial z^2} - \frac{\partial^2 \Psi}{\partial x^2} = 0. \quad (z = H) \quad (4.97)$$

The full stress perturbation perpendicular to the surface must also be zero. This means that at the glacier surface, the deviatoric stress perturbation is (from equation (4.83))

$$\tilde{\tau}_{xx}(x, H) = \frac{1}{2} \tilde{\sigma}_{xx}(x, H). \quad (4.98)$$

At the surface, the perturbation balance equation (4.80) then reduces to

$$2 \frac{\partial \tilde{\tau}_{xx}}{\partial x} + \frac{\partial \tilde{\tau}_{xz}}{\partial z} = 0. \quad (z = H) \quad (4.99)$$

Again, invoking the linear flow law and the definitions of the stream function gives the following boundary condition:

$$3 \frac{\partial^3 \Psi}{\partial x^2 \partial z} + \frac{\partial^3 \Psi}{\partial z^3} = 0. \quad (z = H) \quad (4.100)$$

The four constants a_i appearing in expression (4.94) for the stream function can now be determined from the four boundary conditions (4.92), (4.93), (4.97),

and (4.100). After some tedious arithmetic, the following result is found (Balise, 1988, p.10):

$$a_1 = \frac{-2\omega H^2}{2 + 4\omega^2 H^2 + e^{2\omega H} + e^{-2\omega H}}, \quad (4.101)$$

$$a_2 = \frac{1 - 2\omega H + e^{-2\omega H}}{2 + 4\omega^2 H^2 + e^{2\omega H} + e^{-2\omega H}}, \quad (4.102)$$

$$a_3 = \frac{2\omega H^2}{2 + 4\omega^2 H^2 + e^{2\omega H} + e^{-2\omega H}}, \quad (4.103)$$

$$a_4 = \frac{1 + 2\omega H + e^{-2\omega H}}{2 + 4\omega^2 H^2 + e^{2\omega H} + e^{-2\omega H}}. \quad (4.104)$$

With the stream function known, the two components of velocity can be determined using equation (4.87). Symbolically, the velocities can be written as

$$\tilde{u}(x, z) = F_u(\omega, z) U_b \sin \omega x, \quad (4.105)$$

$$\tilde{w}(x, z) = F_w(\omega, z) U_b \cos \omega x. \quad (4.106)$$

In these expressions, F_u and F_w represent the transfer functions, defined as (Balise, 1988, p.11)

$$F_u(\omega, z) = \omega a_1 e^{\omega z} - \omega a_3 e^{-\omega z} + (a_2 + a_2 \omega z) e^{\omega z} + (a_4 - a_4 \omega z) e^{-\omega z}, \quad (4.107)$$

and

$$F_w(\omega, z) = \omega a_1 e^{\omega z} + \omega a_3 e^{-\omega z} + a_2 \omega z e^{\omega z} + a_4 \omega z e^{-\omega z}. \quad (4.108)$$

These transfer functions describe how the basal anomaly is attenuated upward to the glacier surface. Because the amplitude of the perturbation decreases going upward toward the glacier surface, the transfer functions are also referred to as filter functions. The transfer functions are independent of the along-flow coordinate, and the amount of filtering (or relative decrease in amplitude) is independent of the amplitude of the basal perturbation. The only important parameter in the transfer functions is the wavelength of the basal perturbation, $L = 2\pi/\omega$. This is illustrated in [Figure 4.10](#), which shows F_u and F_w as a function of the dimensionless wavelength, L/H , and dimensionless depth, z/H .

For wavelengths longer than about 50 ice thicknesses, the basal perturbation attenuates almost undisturbed to the glacier surface. For very short wavelengths, less than about one ice thickness, the perturbation is damped very rapidly going upward in the ice, affecting only the lower 10% of the glacier. For intermediate wavelengths,

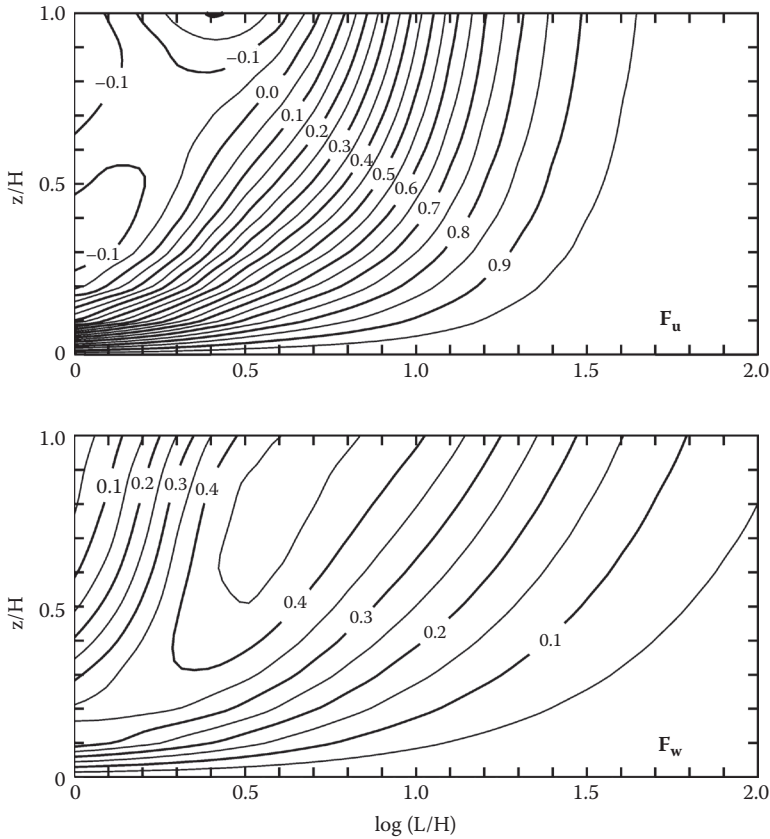


FIGURE 4.10 Transfer (or filter) functions at depth and as a function of the dimensionless wavelength of the harmonic perturbation in the velocity parallel to the bed. F_u represents the transfer function for the horizontal component of velocity and F_w represents the transfer function for the vertical velocity component, both for the case of a linear-viscous glacier.

the transfer of basal perturbations is most complex. This is better illustrated by considering the perturbation velocities at the glacier surface.

The transfer functions evaluated at the surface, $z = H$, are

$$F_u(\omega, H) = \frac{(2 - 2\omega H)e^{\omega H} + (2 + 2\omega H)e^{-\omega H}}{2 + 4\omega^2 H^2 + e^{2\omega H} + e^{-2\omega H}}, \quad (4.109)$$

$$F_w(\omega, H) = \frac{2\omega H e^{\omega H} + 2\omega H e^{-\omega H}}{2 + 4\omega^2 H^2 + e^{2\omega H} + e^{-2\omega H}}. \quad (4.110)$$

These transfer functions are shown in [Figure 4.11](#) and represent the relative amplitude of the surface perturbation velocity, if the amplitude of the basal perturbation is taken equal to unity ($= 1$). Figure 4.11 shows that three different regimes can be

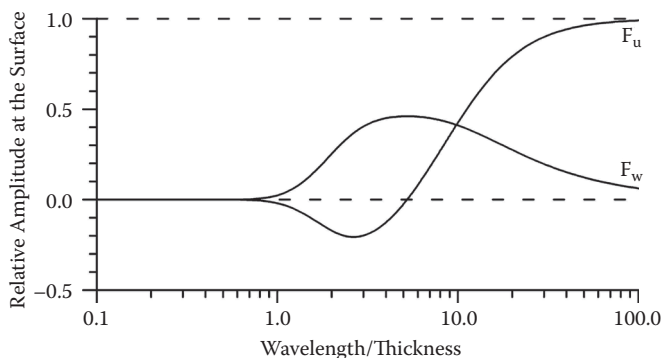


FIGURE 4.11 Surface value of the transfer functions shown in Figure 4.10.

identified, depending on the wavelength of the basal perturbation. For very short wavelengths ($L \leq 0.7 H$), there is no surface expression of the basal perturbation. If the wavelength is comparable to the thickness of the glacier ($0.7 H \leq L \leq 5 H$), the perturbation velocity parallel to the surface has a direction opposite that of the basal perturbation. This effect is largest for $L/H = 2.75$, with the surface velocity about 20% of the basal velocity. The result is a circular motion of the perturbation flow, as shown in Figure 4.12. The velocity perpendicular to the surface reaches a maximum for $L/H \approx 5$, while for this wavelength the surface-parallel component of velocity is zero. For increasing wavelengths larger than five ice thicknesses, the surface expression of the basal perturbation becomes increasingly similar to the basal perturbation, and the velocity anomaly does not recirculate (Balise and Raymond, 1985).

The model used to arrive at expressions for the transfer functions may be criticized, most notably for using a linear viscous rheology. Balise (1988) uses a finite-difference model to investigate how a power-law rheology affects the transfer functions. The main difference between the linear and power-law solutions is that the magnitudes of the nonlinear transfer functions, F_u and F_w , are considerably less than the magnitudes of the corresponding linear transfer functions (4.107) and (4.108). Thus, for a given harmonic variation in the bed-parallel velocity, the nonlinear rheology results in less effect at the glacier surface than with the linear rheology. Interestingly, for a harmonic variation in the component of velocity perpendicular to the glacier bed (w_b), both rheologies produce similar results.

The nonlinear transfer functions are determined by Balise (1988) by prescribing a harmonic basal perturbation of certain wavelength and calculating numerically the surface perturbations. The transfer functions so determined have more limited applicability than their linear counterparts. For a linear rheology, an arbitrary basal variation may be considered the sum of (many) harmonic perturbations. Applying the corresponding linear transfer function to each harmonic component allows the various harmonic surface perturbations to be calculated. Adding these components gives the total perturbation velocity at the surface. This Fourier-transform method is possible because the harmonic perturbations do not interact with each other in the linear model. In the more realistic case of nonlinear ice rheology, the effective

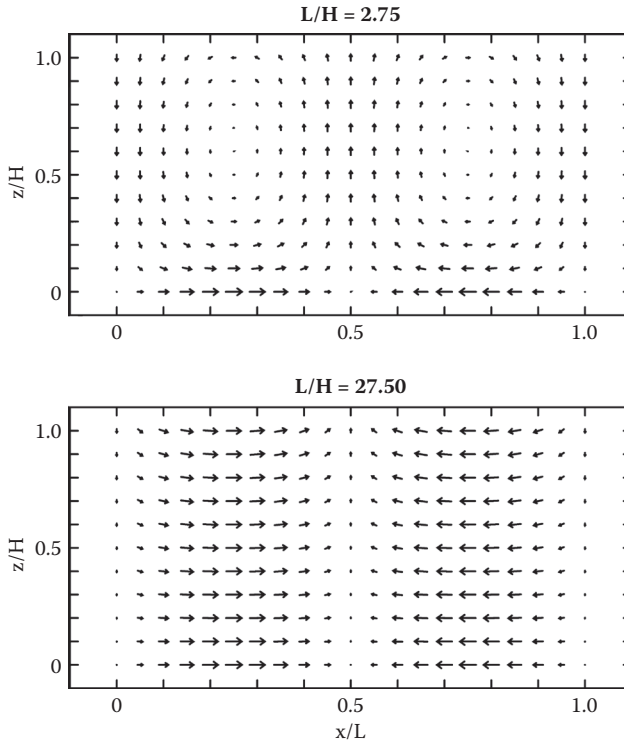


FIGURE 4.12 Pattern of perturbation flow for a short-wavelength (upper panel) and long-wavelength (lower panel) harmonic perturbation in the velocity parallel to the glacier bed.

strain rate depends on all other strain rates and each harmonic component influences all others. In addition, the large-scale flow also affects the perturbation flow. This means that each situation needs to be studied separately, using numerical techniques to solve the nonlinear equations for the complete velocity and stress distributions (Balise, 1988).

A further objection against the model of Balise and Raymond (1985) may be its simple geometry that does not allow for variations in the upper and lower glacier surfaces. As shown by Whillans and Johnsen (1983), perturbations in geometry can be included, by retaining the full form (4.89) of the stream function and imposing additional boundary conditions. Their analysis indicates that sliding variations on a flat bed may lead to important surface relief. For sliding variations with a wavelength of about three ice thicknesses, Whillans and Johnsen (1983) find flow variations similar to those shown in Figure 4.12 ($L/H = 2.75$), with the surface undulation out of phase with the basal variation. That is, where the velocity perpendicular to the surface is directed outward, a surface high occurs, while a surface low is found where this velocity is directed into the glacier.

The main reason for discussing the earlier analyses of Whillans and Johnsen (1983), Balise and Raymond (1985), and Balise (1988) in some detail is their relative

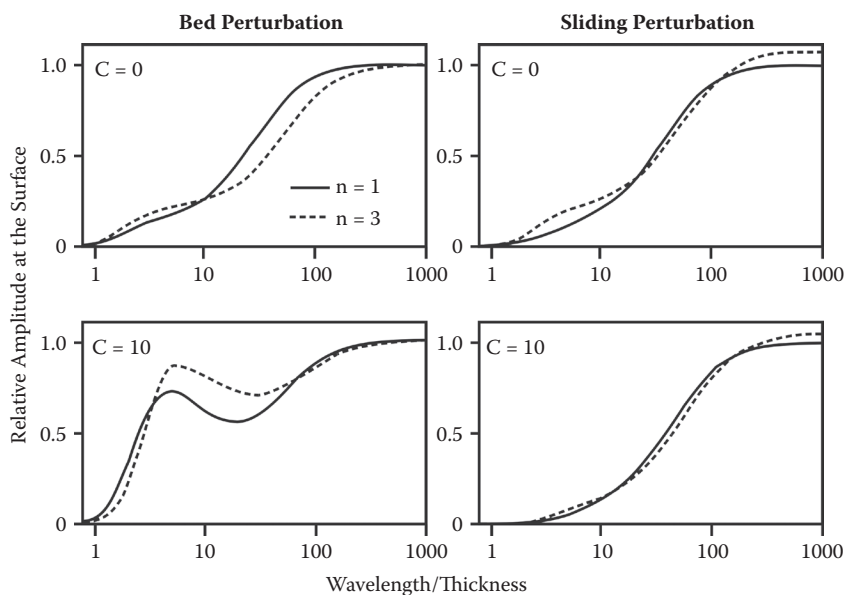


FIGURE 4.13 Relative amplitude of surface topography for a perturbation in basal topography (left panels) and sliding perturbation (right panels), for the case of no or little sliding (upper panels) and for large basal sliding (lower panels), and for linear ($n = 1$) and nonlinear ($n = 3$) ice rheology. (From Raymond, M. J., and G. H. Gudmundsson, *J. Geoph. Res.*, 110, B08411, 2005. Copyright by the American Geophysical Union.)

simplicity. More recent treatments are perhaps more rigorous but are also of greater mathematical complexity, which may obscure the underlying physics. For example, Gudmundsson (2008) presents analytical solutions describing the effects of perturbations in basal boundary conditions for ice streams moving over soft sediment. Linear viscosity is assumed for the ice. Scaling is applied to the governing momentum equations to arrive at a system of equations that is solved using Fourier and Laplace methods. While in detail, the conclusions from that analysis and similar recent ones differ from earlier studies, from the perspective of using surface measurements to infer conditions at the glacier bed, the conclusions are similar, namely, that short-scale variations at the glacier bed are difficult to detect at the glacier surface, if not completely absent.

Figures 4.13 and 4.14 show transfer functions obtained by Raymond and Gudmundsson (2005) using finite-element solutions to the full momentum equations for both linear ($n = 1$) and nonlinear ($n = 3$) ice rheology. Perturbations in bed topography (panels on the left) or basal sliding (panels on the right) were prescribed, and their effect on surface topography (Figure 4.13) and surface speed (Figure 4.14) was investigated in the absence of significant basal motion ($C = 0$ or 1; upper panels) and for the case of large sliding ($C = 10$; lower panels). For sliding variations the transfer functions for both the surface topography and surface velocity increase steadily with wavelength of the perturbation. For transfer of basal topographic variations to the surface, three spatial scales should be considered as also suggested by the transfer

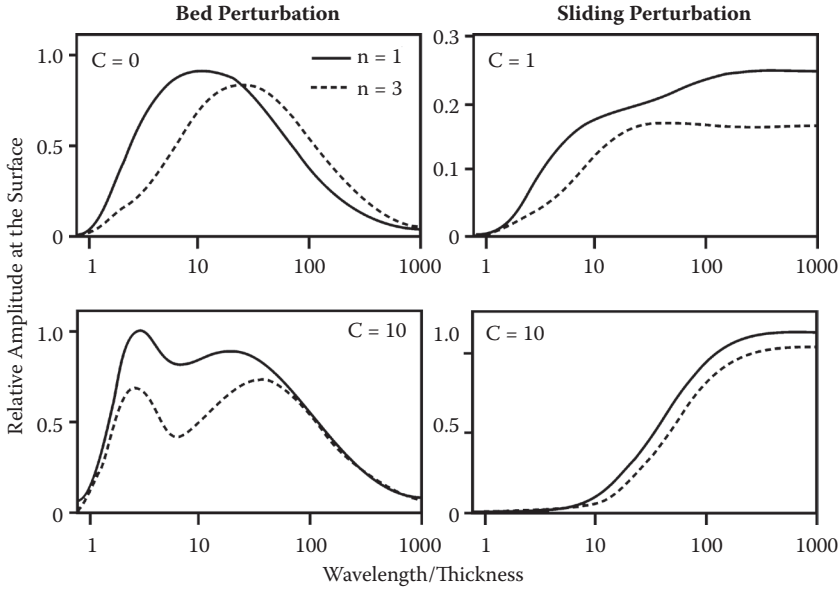


FIGURE 4.14 Relative amplitude of surface velocity for a perturbation in basal topography (left panels) and sliding perturbation (right panels), for the case of no or little sliding (upper panels) and for large basal sliding (lower panels), and for linear ($n = 1$) and nonlinear ($n = 3$) ice rheology. (From Raymond, M. J., and G. H. Gudmundsson, *J. Geoph. Res.*, 110, B08411, 2005. Copyright by the American Geophysical Union.)

functions shown in Figure 4.11. On short scales (wavelength less than about three ice thicknesses), surface expressions of basal perturbations are small, more so when nonlinear rheology is assumed. When basal sliding is zero, the transfer function for surface topography (Figure 4.13, upper left panel) increases rapidly for intermediate wavelengths and reaches unity for long wavelengths. Where sliding is important, this transfer function reaches a maximum at about seven ice thicknesses, then decreases, and increases again for longer wavelengths (Figure 4.13, lower left panel). The associated perturbation in surface velocity reaches a maximum for intermediate wavelengths and decreases to zero for long wavelengths (Figure 4.14, left panels). This behavior likely reflects that for very short perturbations, flow anomalies are concentrated in the basal layers, while for very long perturbations, the ice can simply follow the bed topography without adjusting its flow. At intermediate scales, longitudinal stresses and other flow interactions lead to the greatest surface expression.

The implication is that basal perturbations with spatial scales of less than about one ice thickness cannot be detected using surface measurements. Also, small errors in measured surface velocities may lead to unrealistically large variations in sliding velocity. Consider, for example, the situation in which surface measurements are spaced one ice thickness apart. If the uncertainty in surface velocity is, say, 1 cm/yr, the corresponding error in basal velocity is about 90 cm/yr. Increasing the

measurement interval to two ice thicknesses would reduce the error in basal velocity to about 6 cm/yr. Achieving a similar accuracy by making more precise surface measurements at the original spacing of one ice thickness would require a reduction in the measurement error to less than 1 mm/yr. Such an accuracy cannot be accomplished in many cases.

While the discussion in this section focuses on the transfer of basal variations to the glacier surface, these theories and models can also be used to explain observed variations in internal layers detected by radar. For example, Whillans and Johnsen (1983) apply their model to the Byrd Station Strain Network, West Antarctica, and find that the phase relationship between internal layer distortion and surface topography agrees with model predictions, while Whillans and Jezek (1987) successfully apply a similar theoretical model to explain folding of internal layers along the Dye-3 strain grid. Hindmarsh and others (2006) develop a mechanical theory to show that where wavelengths of basal topography are comparable with or less than the ice thickness, internal layers tend to override the basal topography with layers above topographic highs being essentially flat. For longer wavelengths, internal layers are draped over the topography, with the layers essentially following the bed topography. For the most part, however, the use of internal layer structure has not been widely used in glaciology to constrain or validate theoretical and numerical models.

4.7 FLOW NEAR AN ICE DIVIDE

Most deep-ice-drilling programs, aimed at obtaining long paleoclimatic records, are conducted at or near ice divides on ice caps. The rationale is that, provided the divide has not migrated in the past, ice at the divide is not affected by horizontal flow and may be assumed to have originated at the same location. This means that variations with depth of parameters measured in the core, such as annual layer thickness or isotope concentration, reflect temporal changes in the local climate conditions (precipitation, temperature, etc.). In contrast, for a drilling site removed from the divide, there is a need to model ice flow, including past history, along the flowline extending from the divide to the drilling location. The lack of horizontal perturbations to flow at the divide often outweighs the problems associated with establishing an accurate depth-age scale for an ice divide. The reason for this difficulty is that conventional models for glacier flow, in particular the lamellar flow theory (Section 4.2), do not apply to the divide region where the vertical shear stress vanishes.

The ice divide, or flow divide, is defined as the plane extending from the base to the surface, through which there is no transport of mass. The ice crest is the location where surface elevation is highest. Thus, the divide separates ice flowing in opposite directions. On smaller ice caps or at local ice domes that are spreading radially, the divide reduces to a single line from surface to bed. In the absence of basal topography, or where a bed topographic high underlies the ice crest, the flow divide occurs at the highest surface elevation (Figure 4.15, upper panel). However, most divides are not symmetric because there may be a gradient in net accumulation across the ice sheet, or because of an asymmetric basal topography. In that case, the flow divide and ice crest are co-located at the surface only, but the divide plane slopes such that

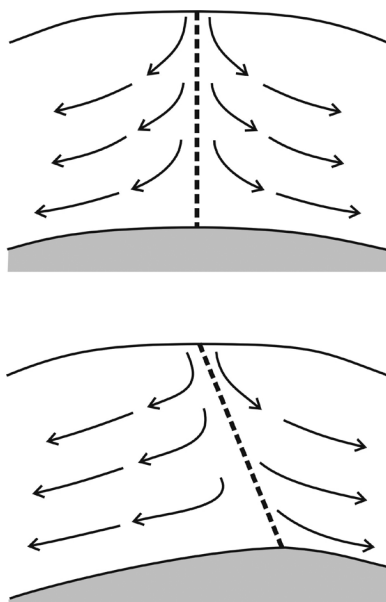


FIGURE 4.15 Illustrating different ice divide geometries. Where the bed topography is symmetric around the vertical line through the ice crest (highest surface elevation), the ice divide (or flow divide) is also vertical (dashed line in upper panel). Where the bed topography is asymmetric, the ice divide is generally sloping and coincides with the ice crest only at the surface (dashed line, lower panel).

the flow divide at the base does not directly underly that at the surface (Figure 4.15, lower panel).

The distribution of stresses and velocities near an ice divide has been discussed in a number of studies using numerical methods to solve the full balance equations (Raymond, 1983; Paterson and Waddington, 1984; Reeh and Paterson, 1988; Dahl-Jensen, 1989; Szidarovsky et al., 1989; Hvidberg, 1996). The main conclusion that can be drawn from these studies is that the divide region is relatively small. At a distance of about four ice thicknesses from the divide, flow on the flank is adequately described by the lamellar flow assumption. Following Raymond (1983) an approximate analytical solution can be derived.

For an isothermal divide on a horizontal bed, model results show that at the divide the vertical velocity varies approximately parabolically with depth and

$$w(s) = w(0)(1 - s)^2, \quad (4.111)$$

with $w(0)$ the vertical velocity at the surface ($s = 0$). For steady state, this velocity must balance the accumulation rate and thus the vertical velocity is negative throughout the column, decreasing to zero at the bed (neglecting basal melting). The corresponding vertical strain rate is

$$\dot{\epsilon}_{zz} = 2 \frac{w(0)}{H} s, \quad (4.112)$$

and increases linearly from zero at the surface to the maximum value at the bed. Note that $w(0)/H$ represents the depth-averaged strain rate, that is, the difference between the vertical velocity at the surface and at the bed, divided by the ice thickness.

Incompressibility dictates that the horizontal stretching rate equals minus the vertical strain rate. With the horizontal velocity being zero at the ice divide ($x = 0$), integrating equation (4.112) with respect to x and adding a minus sign gives the vertical profile of the horizontal velocity

$$u(s) = u(0)(1 - s). \quad (4.113)$$

In the integration, the ice thickness is kept constant, and thus small variations in geometry in the vicinity of the divide are neglected. The horizontal velocity at the surface increases with distance from the divide as

$$u(0) = -2 \frac{w(0)}{H} x. \quad (4.114)$$

Because the vertical velocity is directed downward ($w(0) < 0$), the horizontal velocity is positive.

A comparison between the divide solution and the lamellar flow solution is shown in Figure 4.16. Because the horizontal velocity varies linearly with depth in the divide region, vertical shear is uniform throughout the column and the normalized velocity is smaller than on the flank. In contrast, the normalized vertical velocity in the divide region is greater than on the flank. While differences in the two profiles of the vertical velocity shown in the right panel of Figure 4.16 are less pronounced than

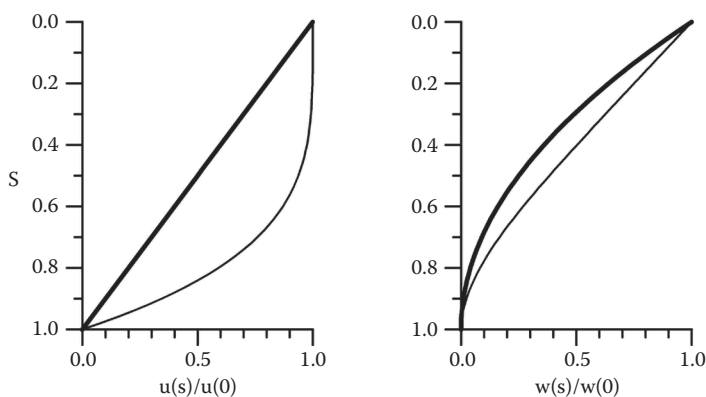


FIGURE 4.16 Horizontal (left panel) and vertical (right panel) component of velocity scaled to the surface velocity, as a function of dimensionless depth, for the approximate divide solution (heavy curves) and the lamellar flow solution (light curves).

those in the profiles in the horizontal velocity, this difference has interesting consequences for the shape of isochrones (layers of constant age) in the divide region.

The left panel in Figure 4.17 shows the vertical thinning rate, $\dot{\epsilon}_{zz}$, and shows that thinning of layers occurs more uniformly with depth at the ice divide than on the flanks, where thinning is greatest in the upper half of the glaciers, and rapidly decreases near the bottom. As a result, downward flow is impeded at the divide, and ice at a given depth will be of younger age than ice at the same depth on the flank. To quantify this difference, the age of the ice at depth can be estimated from

$$a(s) = \int_0^s \frac{H}{w(\bar{s})} d\bar{s}. \quad (4.115)$$

Integrating this expression gives

$$a(s) = \frac{H}{w(0)} \frac{1}{1-s}. \quad (4.116)$$

For the lamellar flow solution (4.31), the integral is more complex and estimated from numerical integration. The right panel in Figure 4.17 shows both age-depth relations. Note that these results apply only to an ice divide that has been stationary and with constant thickness and accumulation rate, which probably are not very realistic assumptions for real divide regions.

On the flank, ice moves downward more quickly than near the divide, producing local upward arches in isochrones under the divide, called Raymond bumps. Such bumps have been observed in radar-sounding records (that record internal stratigraphic layers) in several locations including Fletcher Promontory, a large ice rise on the Ronne Ice Shelf, West Antarctica (Vaughan et al., 1999); on Siple Dome, a large ice dome adjacent to the Ross Ice Shelf and separating Kamb

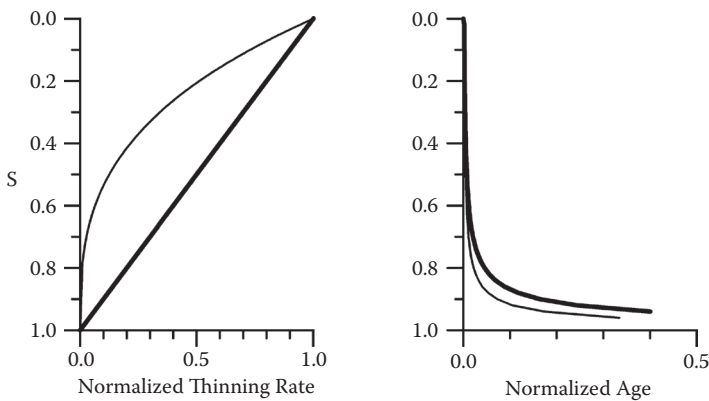


FIGURE 4.17 Normalized thinning rate (left panel) and normalized age (right panel) as a function of dimensionless depth, for the approximate divide solution (heavy curves) and the lamellar flow solution (light curves).

and Echelmeyer ice streams (Nereson et al., 1998); and on Roosevelt Island on the Ross Ice Shelf (Conway et al., 1999). Radar transects across the divide in Greenland do not show such upwarping arches (Jacobel and Hodge, 1995), which may be because the divide migrated during the last glacial cycle (Marshall and Cuffey, 2000).

The Raymond (1983) model applies to isothermal flow in the vicinity of an ice divide. Since that study, several investigations have been carried out to investigate the importance of ice temperature, ice rheology, and divide migration on isochrone geometry. Reduced downward advection of cold surface ice may keep the basal ice under the divide warmer than away from the divide, thereby softening the ice. The model results of Hvidberg (1996) suggest that this thermal softening lowers the amplitude of the Raymond bumps.

Further refinements to modeling divide flow have been made. Pettit and Waddington (2003) argue that at low deviatoric stresses found near divides, a linear flow law is more appropriate than the usual Glen's law with exponent $n = 3$. Their model results indicate that adopting a linear flow law yields velocity profiles that are similar at the divide and at the flank so that internal layers or isochrones do not show the Raymond bump. Pettit et al. (2007) further investigated the role of crystal fabric, recognizing that near an ice divide, a preferred crystal fabric with c -axes clustered vertically is often found. Such a fabric tends to increase the amplitude of the Raymond bump. The model of Martin et al. (2009) applies to isothermal conditions but includes calculation of fabric development induced by ice deformation, and a nonlinear anisotropic flow law. Their model produces a number of features observed in radar echograms, including concave surface undulations on both sides of the divide, synclines in isochrones on both sides of the Raymond bumps, and double-peaked Raymond bumps close to the bed.

